Aeroacoustic-Source Analysis of a Structured Porous Coated Cylinder

Original
Aeroacoustic-Source Analysis of a Structured Porous Coated Cylinder / Burruni, F., Zarri, A., Zamponi, R., Avallone, F., Arcondoulis, E.J.G.. - (2026). (32nd AIAA/CEAS Aeroacoustics Conference (2026) Brussels (BEL) 26-29 May 2026) [10.2514/6.2026-3568].

Publisher:
American Institute of Aeronautics and Astronautics

Published
DOI:10.2514/6.2026-3568

Aeroacoustic Source Analysis of a Structured Porous-Coated Cylinder

Francesco Burruni*[1], Riccardo Zamponi†[2,3], Elias J. G. Arcondoulis ‡[4], Alessandro Zarri§[2], and Francesco Avallone¶[1]
[1]*Politecnico di Torino, Corso Duca degli Abruzzi 24, 10129 Torino, Italy*
[2]*von Karman Institute for Fluid Dynamics, Waterloosesteenweg 72, B-1640 Sint-Genesius-Rode, Belgium*
[3]*Delft University of Technology, 2629HS Delft, The Netherlands*
[4]*University of Southampton, SO17 1BJ Southampton, UK*

Among passive noise control strategies, the use of porous coatings around bluff bodies, such as circular cylinders, has been widely investigated in recent years. In the present work, a high-fidelity simulation based on the lattice-Boltzmann method has been employed to elucidate the noise generation mechanisms of a Structured Porous Coating. The results show that the acoustic field is dominated by high-frequency noise generated by the small-scale cylinders that constitutes the porous medium. In the low-frequency range, although the flow Mach number is low, the dominant noise contribution originates from wake sources. This finding enables an equivalent interpretation of cylinder noise as a diffraction problem. Indeed, the porous coating induces an increase of the vortex formation length, which displaces the quadrupolar source at the onset of vortex shedding further downstream and consequently diminishes the efficiency of the sound scattered by diffraction from the body surface. The relevance of wake sources is further confirmed through an alternative approach based on coherence analysis. These results are consistent with recent experimental evidence highlighting the significant role played by wake sources in porous cylinders, even at low Mach numbers.

I. Introduction

The aerodynamic noise radiated by the flow past a circular cylinder is relevant in many environmental and engineering applications, such as landing gear systems and high-speed train pantographs. When a circular cylinder is immersed in a crossflow, above a critical Reynolds number, a periodic detachment of vortical structures occurs from the cylinder surface, giving rise to the well-known von Kármán vortex street [1]. This process, referred to as vortex shedding, generates a characteristic tonal noise known as the Aeolian tone. The shedding of vortices induces a fluctuating hydrodynamic force on the cylinder, which in turn acts as a source of acoustic radiation in the surrounding fluid.

Minimizing the unsteadiness of the von Kármán vortex street can have beneficial effects in terms of noise suppression. In this regard, one passive control strategy is to coat the cylinder surface with a porous material. Sueky et al. [2] were the first to experimentally demonstrate the beneficial effects of the porous coating in terms of noise reduction. Additionally, Liu et al. [3] found a narrowing and a shift toward lower frequencies of the tonal peak in the Sound Pressure Level (SPL) spectrum. These results were also confirmed by Geyer and Sarradj [4], who found that the best performance in terms of noise reduction is achieved with porous media characterized by high air-flow permeability.

Regarding the effects of the porous medium on the wake pattern, Sadeghipour et al. [5] found that, in a porous configuration, the recirculation region is shifted downstream, and this effect is more pronounced for the most flow-permeable cover. The same results were also observed by Showkat Ali et al. [6] and Xia et al. [7], who noted a downstream shift of the onset of vortex shedding, an increase in the so-called vortex-formation length, and a reduction in the energy content in the near-wake region. Naito and Fukagata [8] explained that these flow-field alterations are related to the presence of a slip velocity inside the porous medium and to the strong energy dissipation encountered by the flow as it penetrates the porous medium. The combination of these effects results in more stable shear layers and weaker mutual interaction between them. Sato and Hattori [9] physically linked noise mitigation to the presence of a fluid region within the porous medium and a nearly uniform pressure profile in the wake. According to the authors, these two factors help stabilize the wake and suppress unsteady vortex motion.

Porous coatings can be realized in various ways to control both structural and acoustic properties. Arcondoulis et al. [10] developed a 3D-printed Structured Porous Coating (SPC) in which parameters such as airflow permeability and porosity can be readily tailored. They demonstrated that SPC provides noise-reduction performance comparable to that of conventional open-cell porous materials, which possess a randomized internal geometry but share equivalent macroscopic parameters. The use of an SPC enables a more detailed investigation of the flow pattern within the porous medium [11].

Specifically, previous studies have shown that SPC effectively reduces the amplitude of the vortex-shedding tone and low-frequency broadband noise. However, a clear drawback is the emergence of a high-frequency acoustic contribution. Through high-fidelity simulations, Kong et al. [12] observed that vortex shedding occurring around the structural elements of the porous medium contributes to stabilizing the overall vortex-shedding process and is the primary source of this broadband mid-to-high-frequency noise. This result was confirmed by the analytical model of Arcondoulis et al. [13], which was based on modeling the internal potential flow within the porous medium by Zamponi et al. [14] and demonstrated that, at high frequencies, the dominant noise sources are located in the windward region around the cylinder surface.

Despite numerous studies, the physical link between flow-field alterations and the associated noise mitigation achieved by porous coatings is not yet fully clarified, nor are the mechanisms responsible for the observed noise increase at high frequencies. This work aims to fill this gap by investigating the nature and location of the dominant aeroacoustic sources in a porous-coated cylinder throughout the frequency range. The need for such an analysis is motivated by the experimental evidence recently provided by Zamponi et al. [15], which demonstrated that, at low frequencies, the dominant sound sources in a porous-coated cylinder are not located on the surface of the porous body but rather in its wake, at the onset of the vortex-shedding instability. These results challenge the common assumption that cylinder noise is generated solely by the fluctuating force exerted by the body on the surrounding fluid, while the volume terms in the wake are negligible, and open new possibilities for the design of innovative noise-mitigation strategies for cylinder flow-induced noise [16]. In that study, the authors proposed a simple analytical model based on the formulation of the radiated sound as a diffraction problem to support the experimental results, but further investigations are required to confirm this scenario. The aeroacoustic source analysis presented in this paper is based on a high-fidelity simulation using the Lattice Boltzmann Method (LBM) of the flow past a fully resolved structured porous-coated cylinder, whose design was inspired by the work of Wen et al. [17].

This document is organized as follows. In Section II, a theoretical description of the sound radiated by the flow past a porous-coated cylinder is outlined. In Section III, the computational setup and post-processing parameters are presented, whereas, in Section IV, the grid comparison is performed. The aerodynamic and aeroacoustic results are presented and analyzed in Section V. Finally, preliminary conclusions are drawn in Section VI.

II. Theory

A. Formulation of cylinder flow-induced noise

This section provides the theoretical background concerning the sound-production mechanisms in an SPC. As discussed in Section I, the aerodynamic noise produced by the flow past a circular cylinder in crossflow can be interpreted, in equivalent terms, as the sound radiated from volume sources in the wake, which are subsequently scattered by the cylinder surface. This mechanism becomes particularly effective when the characteristic dimensions of the body are small compared to the acoustic wavelength, i.e., in the acoustically compact limit [18]. Given the pseudo-periodicity of this problem, the formulation is presented in the frequency domain, and a 2D approach is used, despite the wake downstream of the cylinder being intrinsically three-dimensional [19].

Starting from the inhomogeneous Helmholtz equation in the frequency domain:

$$(\nabla^2 - k^2)\,\hat{p}(\mathbf{x}, t) = \hat{q}(\mathbf{x}, t), \tag{1}$$

where $k = \omega/c_0$ is the acoustic wavenumber, ω and c_0 are the angular frequency and speed of sound, respectively. $\hat{p}$ is the acoustic pressure in the frequency domain, $\mathbf{x}$ denotes the position of the observer (Fig. 1) and $\hat{q}(\mathbf{x}, t)$ is the source term. The above equation can be solved by convolution with the Green's function in the frequency domain, which, for a point source located at $\mathbf{y}$, satisfies the following governing equation:

$$(\nabla^2 - k^2)\,\hat{G}(\mathbf{x}, t) = \delta(\mathbf{x} - \mathbf{y}), \tag{2}$$

δ being the Dirac delta function. By means of Green's formalism, the solution of Eq. (1) is:

$$\hat{p}(\mathbf{x}, \omega) = \frac{1}{c_0^2} \iiint_V \frac{\partial^2 \hat{q}(\mathbf{y}, \omega)}{\partial y_i\, \partial y_j}\, \hat{G}(\mathbf{x} \mid \mathbf{y}, \omega)\, dV + \iint_S \left[\hat{G}(\mathbf{x} \mid \mathbf{y}, \omega) \frac{\partial \hat{p}}{\partial y_i} - \hat{p}(\mathbf{y}, \omega) \frac{\partial \hat{G}(\mathbf{x} \mid \mathbf{y}, \omega)}{\partial y_i} \right] n_i\, dS, \tag{3}$$

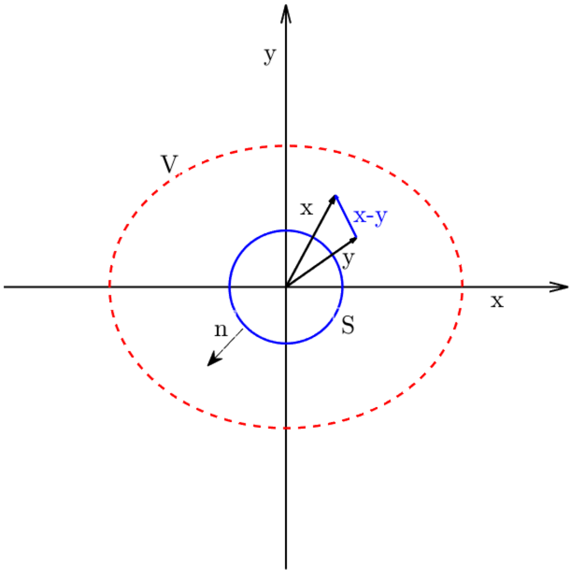

Fig. 1 Coordinate system for the formulation of noise past a circular cylinder.

where S is the body surface and V is an arbitrary volume enclosing the body (see Fig. 1). The source term $\hat{q}(\mathbf{x}, t)$ can be written as:

$$\hat{q}(\mathbf{x}, t) = \frac{\partial^2 \hat{T}_{ij}}{\partial x_i \, \partial x_j}, \tag{4}$$

where $\hat{T}_{ij}$ is Lighthill's tensor [20] in the frequency domain, given by $T_{ij} = \rho \, u_i \, u_j + (p - c_\infty^2 \, \rho') \, \delta_{ij} - \tau_{ij}$, where p, ρ, u_i, u_j, and τ_{ij} are the pressure, density, velocity components, and viscous stress tensor, respectively. The latter term can be neglected because of the high Reynolds number. Consequently, the solution reads:

$$\hat{p}(\mathbf{x}, \omega) = -\iiint_V \hat{T}_{ij}(\mathbf{y}, \omega) \frac{\partial^2 \hat{G}(\mathbf{x} \mid \mathbf{y}, \omega)}{\partial y_i \, \partial y_j} \, dV + \iint_S \Bigg[\hat{G}(\mathbf{x} \mid \mathbf{y}, \omega) \frac{\partial \left(\hat{p} \, \delta_{ij} + \rho \, (\hat{u}_i \hat{u}_j) \right)}{\partial y_i} - \left(\hat{p} \, \delta_{ij} + \rho \, (\hat{u}_i \hat{u}_j) \right) \frac{\partial \hat{G}(\mathbf{x} \mid \mathbf{y}, \omega)}{\partial y_j} \Bigg] n_i \, dS. \tag{5}$$

For a solid, non-vibrating body, u_i and $\frac{\partial p}{\partial n}$ on the surface are both zero due to the no-slip and rigidity conditions, respectively. Equation (5) then becomes:

$$\hat{p}(\mathbf{x}, \omega) = -\iiint_V \hat{T}_{ij}(\mathbf{y}, \omega) \frac{\partial^2 \hat{G}(\mathbf{x} \mid \mathbf{y}, \omega)}{\partial y_i \, \partial y_j} \, dV - \iint_S \left[\hat{p} \, \frac{\partial \hat{G}(\mathbf{x} \mid \mathbf{y}, \omega)}{\partial y_j} \right] n_i \, dS. \tag{6}$$

Substituting the free-field Green function in the frequency domain, $\hat{G}_0$, the Curle's analogy [21] is recovered:

$$\hat{p}(\mathbf{x}, \omega) = -\iiint_V \hat{T}_{ij}(\mathbf{y}, \omega) \frac{\partial^2 \hat{G}_0(\mathbf{x} \mid \mathbf{y}, \omega)}{\partial y_i \, \partial y_j} \, dV - \iint_S \left[\hat{p} \, \frac{\partial \hat{G}_0(\mathbf{x} \mid \mathbf{y}, \omega)}{\partial y_j} \right] n_i \, dS. \tag{7}$$

From the above equation, the first term represents the aerodynamically generated sound. Due to the presence of the second-order derivative, it exhibits a quadrupolar directivity pattern [20]. The second term, on the other hand, accounts for the scattering of acoustic waves by the surface, resulting in a dipole-like field. However, a tailored Green's function in the frequency domain, $\hat{G}_1$, such that $\frac{\partial \hat{G}_1}{\partial n} = 0$ on the cylinder surface, can be considered. Consequently, Eq. (7) becomes:

$$\hat{p}(\mathbf{x}, \omega) = -\iiint_V \hat{T}_{ij} \, \frac{\partial^2 \hat{G}_1(\mathbf{x} \mid \mathbf{y}, \omega)}{\partial y_i \, \partial y_j} \, dV. \tag{8}$$

The tailored Green's function $\hat{G}_1$ can be defined by adding a correction term to the free-field Green's function $\hat{G}_0$, which accounts for the presence of the body and satisfies the prescribed boundary condition, i.e., $\hat{G}_1 = \hat{G}_0 + \hat{G}_s$. A comparison between Eq. (7) and Eq. (8) shows that:

$$\iiint_V \hat{T}_{ij} \frac{\partial^2 \hat{G}_s}{\partial y_i \, \partial y_j} \, dV = \iint_S \left[\hat{p} \, \frac{\partial \hat{G}_0}{\partial y_j} \right] n_i \, dS. \tag{9}$$

The surface term in Curle's analogy can be physically interpreted as the component of aerodynamic noise produced by a volumetric wake source that is scattered by the body. It should be noted that the presence of a porous medium can affect the characteristics of Curle's dipolar sources [22], but this effect is not taken into account in the present study.

B. High-frequency noise-generation mechanism for an SPC

As noted in Section I, the use of an SPC results in a high-frequency broadband contribution arising from the interaction of turbulent flow with the small-scale cylinders of the coating. In this study, it is assumed that the dominant mechanism in this frequency band is small-scale vortex shedding occurring around the structural elements of the SPC [12, 13]. Each structural member of the SPC is assumed to be subject to a local flow field, experience vortex shedding, and consequently generate tonal noise. The uniform distribution of the small-scale cylinders around the bare cylinder makes this mechanism more efficient in an SPC than in a randomized porous medium, such as a porous foam, thereby explaining why the latter provides a more attenuated contribution [10].

To investigate this mechanism, Arcondoulis et al. [13] developed a potential-flow-based mathematical model to estimate the velocity at the outer diameter. Combined with the diameter of the small-scale cylinders in the outermost layer, this information enables the estimation of their vortex-shedding frequencies and associated acoustic intensities.

III. Methodology

A. Flow solver

The simulation was performed using the commercial software 3DS Simulia PowerFLOW 6-2024. The flow solver, based on LBM, is a discrete representation of the Boltzmann equation, in which particles can assume only discrete velocity directions. In this case, a D3Q19 model is adopted, where the first digit represents the spatial dimension and the second the number of discrete directions. Through a Chapman–Enskog expansion [23], the Navier–Stokes equations can be recovered from the Boltzmann equation, and consequently the mean fluid properties can be obtained. A third-order truncation of the Chapman–Enskog expansion is employed.

The entire simulation domain is discretized into voxels. The lattice also incorporates surfels, i.e., surface elements that arise at the interface where the solid boundary intersects the fluid domain. Consequently, particles are allowed to move from one voxel to another at each time step. During this evolution, three types of interactions are considered: inter-particle collisions, advection, and impacts with solid surfaces. Collectively, these interactions act to restore the system to its equilibrium state. In this regard, the Bhatnagar–Gross–Krook collision model is used [24]. It assumes that, following a collision, particles recover their equilibrium state within a relaxation time, whose order of magnitude is comparable to the collision time. In particle–surface interactions, particles are first gathered by surfels and then reflected back into fluid voxels. During this process, energy and mass are conserved, while momentum exchange gives rise to pressure and friction forces.

As the Reynolds number increases, resolving all scales of motion becomes computationally expensive, and turbulence modeling is required to account for unresolved scales. Therefore, the solver performs a Very Large Eddy Simulation (VLES) incorporating the renormalization group form of the k–ϵ model [25]. Subgrid-scale effects are accounted for by introducing a turbulent relaxation time in addition to the viscous relaxation time. It is assumed that the flow near the body follows the universal law of the wall, coupled with a pressure-gradient extension to compute the skin friction.

B. Computational set-up and porous medium model

The SPC configuration denoted SRS98 by Wen et al. [17] is used in the analysis. It is characterized by an overall porosity of 98%. The porous medium is simulated considering four layers of small cylinders equally spaced by 5° around the bare cylinder. Each layer is composed of 72 cylinders. The diameters of the cylinders increase from the innermost layer ($D_1 = 0.321$ mm) to the outermost layer ($D_4 = 0.417$ mm). The two intermediate diameters are $D_2 = 0.350$ mm and $D_3 = 0.382$ mm. Consequently, the overall thickness of the porous coating is $h/d = 0.25$ and the outer diameter is $D = 1.5\,d$, where d is the bare diameter, whose value is 40 mm. A sketch of the porous medium is shown in the bottom right of Fig. 2. The coordinate reference system is located at the center of the cylinder. The X-axis is defined in the streamwise direction, the Y-axis in the crosswise direction, and the Z-axis in the spanwise direction. The free-stream velocity U_0 is set to 30 m/s and is oriented along the X-axis. The computational domain is modeled as a parallelepiped with dimensions $42.75\,d \times 31.50\,d \times 0.50\,d$. At the inlet, both the free-stream velocity and the static pressure of 101325 Pa are prescribed, while at the top, bottom, and outlet, only the static pressure is defined. Solid walls are treated as no-slip boundaries. Moreover, an acoustic buffer region with a distance of $32\,d$ from the center of the cylinder is included to avoid reflection of acoustic waves at the boundaries. This information is summarized in Fig. 2. Six resolution regions are defined for grid refinement. The finest voxel size is 3.91×10^{-5} m around the porous medium. Then, farther from the body, the voxel size of the resolution regions increases by a factor of 2, and the update frequency halves. The resolution, which is the size of voxels over surfels along the characteristic length, i.e., bare diameter, is set to 1024. A physical time of 0.2 s, corresponding to about 25 vortex shedding cycles, is simulated, with a time-step of 3.33×10^{-5} s. Data are recorded after an initial transient of 0.1 s.

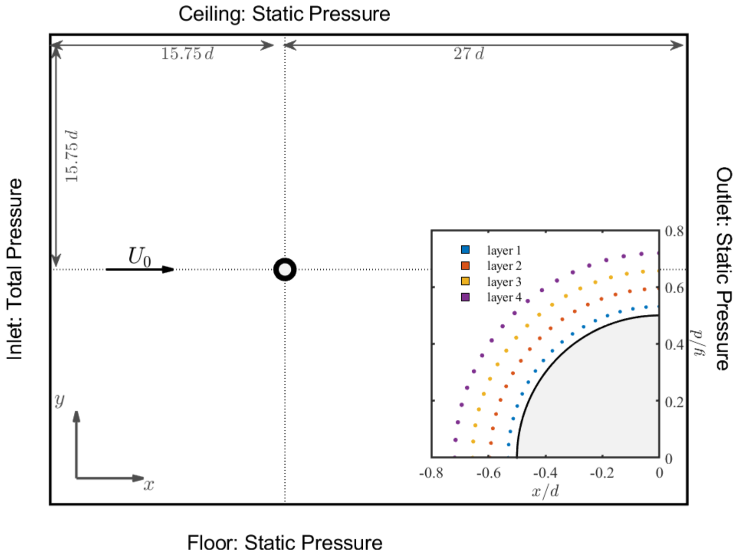

Fig. 2 Numerical set-up of simulation of flow past a porous-coated cylinder. On the bottom right, a sketch of a structured porous medium is reported.

C. Post-processing parameters

Near-field results are used as input for far-field noise calculations based on the Ffowcs-Williams Hawkings (FWH) analogy [26]. In particular, Formulation 1A developed by Farassat and Succi [27] is implemented. Both permeable and solid FWH formulations are considered. The first approach uses a permeable surface that encompasses both the body surface and the near-field region. Thus, both quadrupole and dipole contributions are taken into account. In the second approach, only the surface comprising the flow-permeable cover is considered, and only the dipolar source contribution is taken into account. Acoustic pressure is acquired with a sampling frequency of 29.5 kHz and the Power Spectral Density (PSD) is computed using Welch's method with an FFT window size of 2^{12} and 50% overlap. PSD values, ϕ_p, are referenced to $p_0 = 20\ \mu$Pa as follows:

$$L_p = 10 \log_{10}\left(\frac{\phi_p}{p_0^2}\right). \tag{10}$$

The Overall Sound Pressure Level (OSPL) is computed as

$$L_{p,0} = 10 \log_{10}\left(\sum 10^{L_p/10}\right)\ \text{dB}. \tag{11}$$

For far-field pressure acquisition, virtual microphones are arranged in a circular array at a distance of 25, d from the center of the cylinder, as shown in Fig. 3. The microphones located within the angular range from 60° to −60° have been excluded from the permeable formulation, as, in this region, the acoustic signal is masked by the hydrodynamic contribution of the wake. Moreover, to provide a deeper insight into the relative influence of volume and surface noise sources on the far-field noise, the coherence between far-field pressure and both velocity fluctuations and near-field pressure is calculated as

$$\gamma^2_{a,b} = \frac{\left|\phi_{a,b}(f)\right|^2}{\phi_{a,a}(f)\,\phi_{b,b}(f)}, \tag{12}$$

where $\phi_{a,b}$ is the cross-spectrum between two signals in the time domain (far-field pressure and velocity fluctuations, for instance), whereas $\phi_{a,a}$ and $\phi_{b,b}$ are their PSDs.

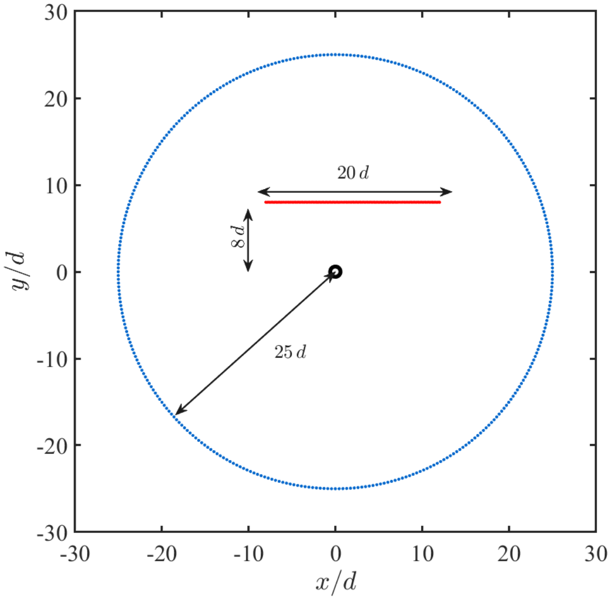

Fig. 3 Virtual microphone arrangement for far-field pressure acquisition.

IV. Comparison against literature

This section evaluates the validity of the present dataset, obtained through LBM simulations, through comparison with the Structure-Resolved Simulations (SRS) reported by Wen et al. [17]. It should be noted, however, that these reference results are derived from a simplified two-dimensional (2D) representation of a structured porous medium and, as such, cannot be considered fully representative for quantitative validation. Future work will address grid convergence by systematically comparing LBM results obtained at different spatial resolutions.

The comparison is performed through an analysis of both the time-averaged streamwise velocity profiles at different x/D locations and the PSD of the aerodynamic forces acting on the cylinder surface. Figure 4 presents the time-averaged streamwise velocity profiles at several stations in the wake. Near the cylinder surface, i.e., at $x/D = 1$ (Fig. 4a), the two curves exhibit nearly identical trends. Only negligible differences are observed in the regions where the velocity reaches its minimum, corresponding to the recirculation zone. A similar trend is observed at $x/D = 2$ (Fig. 4b). At $x/D = 3$ (Fig. 4c), within the recirculation region, both profiles display a Gaussian-like shape. However, the profile obtained from the SRS simulation shows a larger momentum deficit around $y/D = 0$. Finally, at the most downstream section (Fig. 4d), the same pattern as at the previous station is observed.

The slightly larger momentum deficit observed in the SRS data is further confirmed by the streamwise velocity profile along the centerline, reported in Fig. 4e. In the vicinity of the recirculation region, identified by negative velocity values [28], the SRS results exhibit lower velocities than the LBM data.

Finally, the comparison is performed in terms of the PSD of the aerodynamic forces as a function of the Strouhal number, defined based on the free-stream velocity U_0 and the bare cylinder diameter d (Fig. 5). For $St > 0.1$, the drag

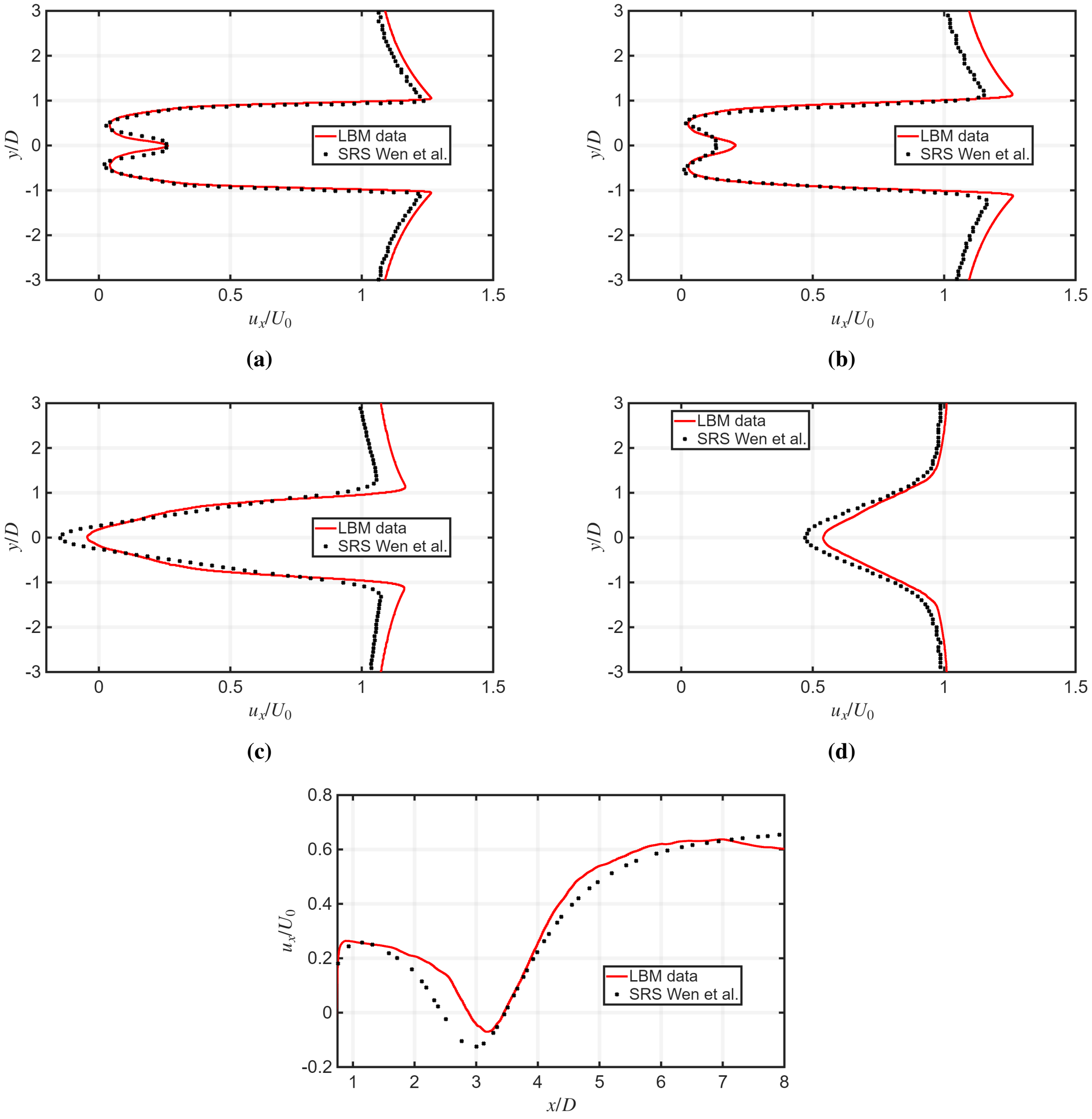

(a)

(b)

(c)

(d)

(e)

Fig. 4 Grid comparison in terms of time-averaged streamwise velocity profiles in the wake of a porous-coated cylinder at different sections: $x/D = 1$ (a), $x/D = 2$ (b), $x/D = 3$ (c), $x/D = 5$ (d), and along the center line (e).

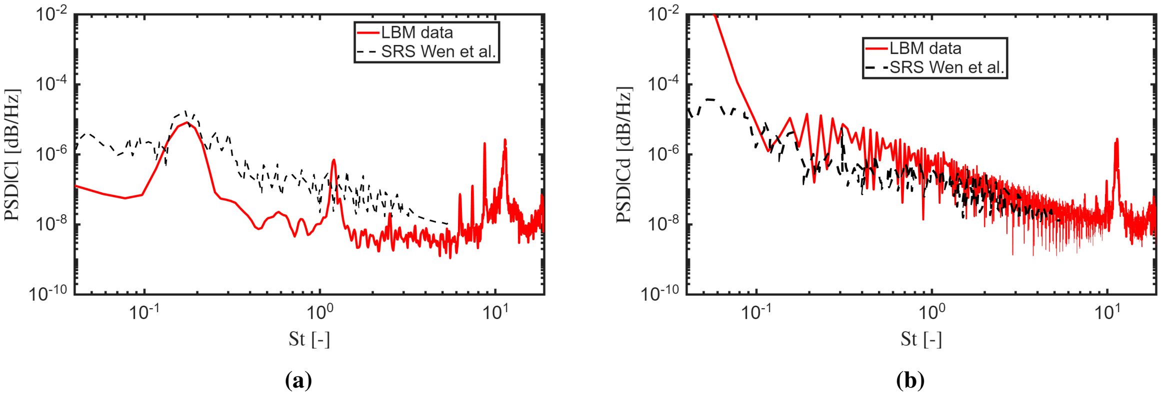

Fig. 5 Grid comparison in terms of PSD of lift (a) and drag (b) coefficients as a function of $St = \frac{fd}{U_0}$.

coefficient spectra show good agreement between the two datasets (Fig. 5b). In contrast, for the lift coefficient (Fig. 5a), the SRS data are higher than those obtained with the LBM data.

V. Results and discussion

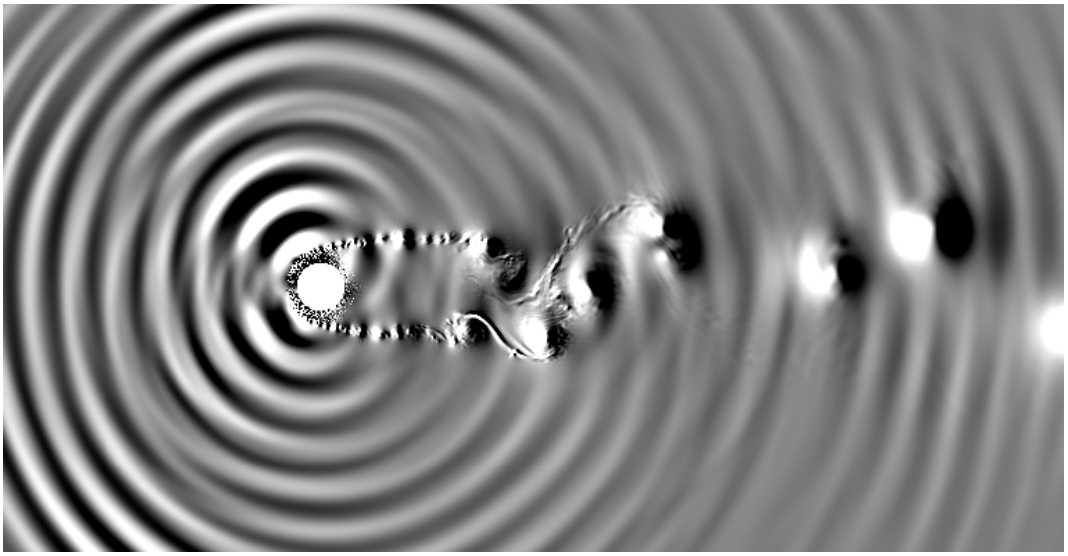

Fig. 6 Instantaneous snapshot of the dilation field $\partial p/\partial t$ induced by a cylinder covered with an SPC.

This section provides an overview of the results obtained from the LBM simulations described in the previous section. First, the radiated flow-induced noise is examined in both the low- and high-frequency bands, highlighting the different sound-generation mechanisms in an SPC. Second, the flow around the body and within the porous medium are analyzed, focusing on flow-field alterations that can physically support the outcome of the aeroacoustic analysis. Finally, a coherence analysis is conducted between far-field acoustic data, velocity fluctuations, and near-field pressure to quantify the relative contributions of volumetric wake sources and surface sources.

A. Aeroacoustic results

An instantaneous snapshot of the dilatation field, i.e., the time derivative of the static pressure, is reported in Fig. 6. The entire field is dominated by a high-frequency contribution originating from the cylinder surface. Moreover, the onset of the vortex shedding instability, which, in the case of a bare cylinder, occurs close to the surface [29], is observed

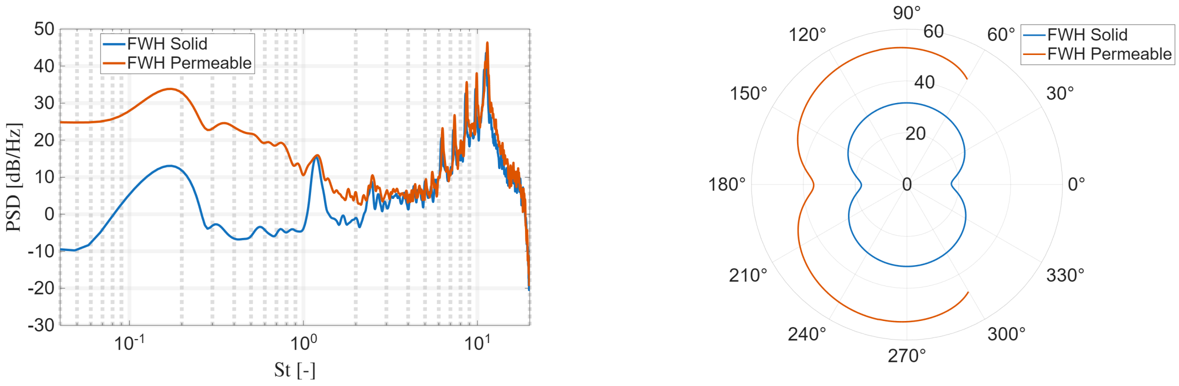

(a) **(b)**

Fig. 7 PSD of far-field pressure based on FWH solid and permeable formulations as a function of $St = fd/U_0$ from the microphone placed at a $\pi/2$ with respect to the reference system in Fig. 2 (a). Directivity plot of the OSPL [dB] considering the microphone array shown in Fig. 3. The integration has been performed up to $St = 1$ (b).

here a few diameters downstream. This effect will be further analyzed in Section V.B.

Figure 7a illustrates the far-field pressure spectrum as a function of the Strouhal number based on the free-stream velocity U_0 and the bare diameter d. A single virtual microphone is considered at the coordinates $x/d = 0$ and $y/d = 25$ according to the reference system shown in Fig. 2. Both permeable and solid FWH formulations are employed. Overall, the acoustic field is dominated by the prominent peak at $St \approx 12$, whose frequency is consistent with the high-frequency acoustic propagation originating from the cylinder surface observed in Fig. 6. Although no direct comparison with a solid cylinder is presented in this study, this behavior is consistent with previous findings suggesting that porous configurations can attenuate low-frequency noise, thereby enhancing the relative contribution of higher-frequency components [10].

In the low-frequency range, i.e., up to $St = 1$, the permeable formulation provides higher SPL values, suggesting that, despite the low Mach number, the acoustic field is dominated by volume sources in the wake. This finding suggests the relevance of quadrupoles in the noise radiated past a porous-coated cylinder. In Fig. 7b, the directivity plot of the OSPL is reported considering the virtual microphone array depicted in Fig. 3. The integration has been performed around the shedding frequency. A gap of more than 20 dB is found between the formulations, confirming the dominant contribution of volumetric wake sources over surface sources. In terms of the equivalent model presented in Section II.A, this result suggests a reduction in the scattering efficiency of the volume sources by the cylinder surface [15, 19] due to the increase in the vortex-formation length induced by the SPC.

A more detailed physical interpretation of the present result is provided in Section V.B. Referring to Fig. 7b, a dipole-like field is obtained using the FWH permeable formulation. This scenario suggests the presence of dominant wake sources exhibiting a dipolar pattern. A quasi-dipolar directivity is also predicted by the equivalent model based on diffraction theory proposed in [15]. The model incorporates a compact lateral quadrupole, located at the position of maximum Turbulent Kinetic Energy (TKE), which acts as an equivalent source representing the aerodynamically generated sound. The sound generated by this source is subsequently scattered by the cylinder surface, leading to the aforementioned quasi-dipolar directivity pattern. From a physical standpoint, the observed dipolar pattern may be associated with the rapid acceleration of vortical structures as they detach from the shear layer. This process may impart a preferential orientation to the equivalent volume sources, which, in an equivalent framework, can be interpreted through diffraction theory. Although this aspect will be further discussed in Section V.B, further investigation is required to fully clarify the underlying physical mechanisms.

At high frequencies, it can be seen that, for $St > 1$, the two formulations provide the same far-field noise, suggesting that, in this regime, the dominant noise originates from the cylinder surface itself. This contribution is associated with the tonal component generated by small-scale cylinders in the windward region, resulting from vortex shedding. This will be further supported by the analysis of the flow-field pattern within the porous medium in Section V.B. This analysis confirms the experimental findings of [15], who showed that, at low frequencies, dominant acoustic sources are located in the wake, while at high frequencies, noise comes from the windward region of the cylinder surface.

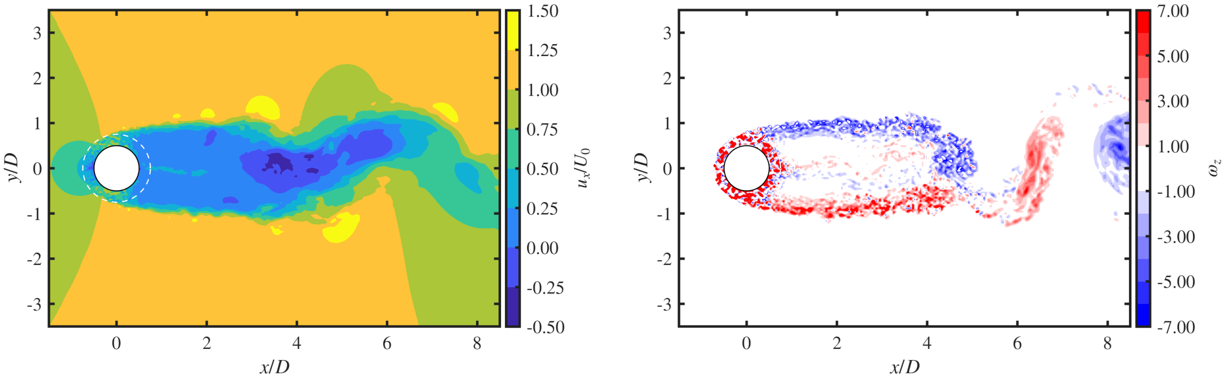

(a) **(b)**

Fig. 8 Instantaneous flow fields: (a) streamwise velocity in dimensionless form based on free-stream velocity U_0; (b) spanwise vorticity in dimensionless form based on U_0 and bare diameter d.

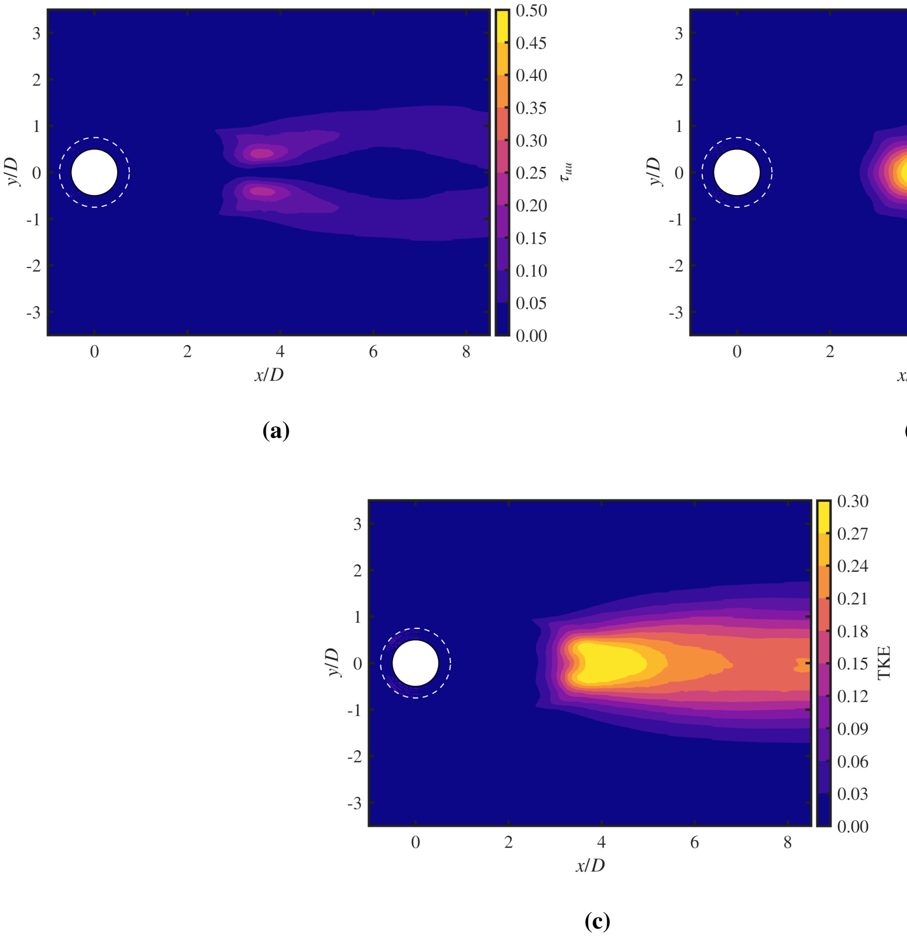

(a) **(b)**

(c)

Fig. 9 Reynolds stresses and turbulent kinetic energy in dimensionless form based on the free-stream velocity U_0: (a) streamwise component τ_{uu}; (b) crosswise component τ_{vv}; (c) TKE.

B. Aerodynamic results

The most prominent effects of the porous coating can be examined through the instantaneous streamwise velocity and spanwise vorticity, shown in Fig. 8a and Fig. 8b, respectively. The streamwise-velocity field highlights the wake broadening through a continuous injection of low-energy fluid into the near wake downstream of the cylinder. This, in turn, leads to a downstream shift of the onset of vortex shedding [5, 7, 15]. Consequently, the flow stabilizes, and the recirculation region is also displaced away from the cylinder surface. Downstream of this region, the periodic detachment of the vortical structures described in Section I begins.

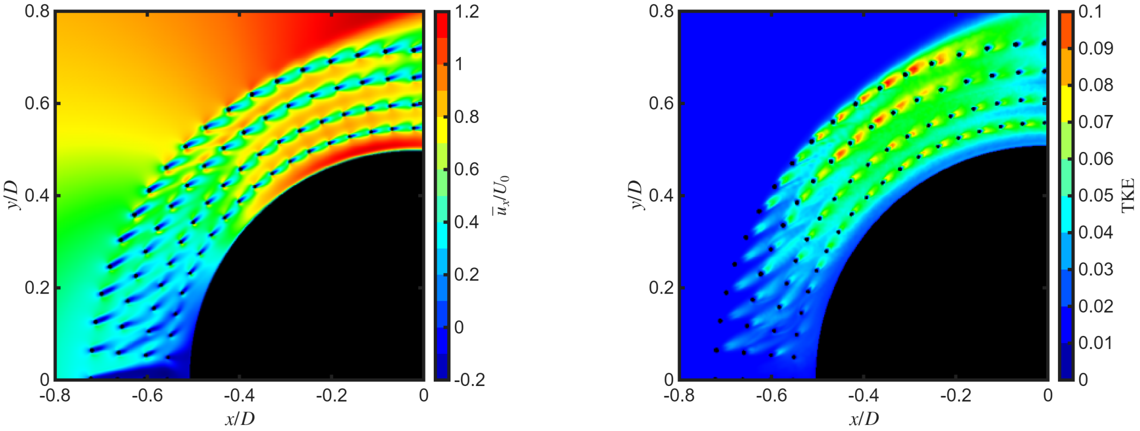

(a) **(b)**

Fig. 10 Detail of time-averaged velocity (a) and TKE (b) in dimensionless form in the windward region of the porous medium.

To better analyze the vortex dynamics described above, the spanwise vorticity field is reported in Fig. 8b. The vortices gradually increase in strength until they are shed into the wake and convected downstream by the mean flow at the end of the vortex-formation region. Consequently, the vorticity experiences rapid acceleration and deformation as it departs from the cylinder's influence. The physical mechanism responsible for the generation of wake sources is likely associated with the interaction of the two counter-rotating vortices when they interact downstream of the vortex formation region.

Referring again to the spanwise vorticity field depicted in Fig. 8b, the shear layers are initially thin and then begin to expand downstream. The transition between these two regions denotes the vortex-formation length. This parameter can be evaluated as the streamwise distance from the cylinder at which the maximum Root Mean Square (RMS) of the vertical velocity fluctuations at $y/D = 0$ occurs [28]. According to this criterion, the vortex-formation length is approximately $x/D \approx 4.5$ in the present case. As anticipated in Section V.A, the increase in the vortex-formation length reduces the efficiency of the scattering mechanism and, consequently, the impact of the surface sources on far-field noise [19].

Moreover, the porous coating has an effect on the Reynolds stress distribution. At high Reynolds numbers and with the assumption of isentropic and incompressible flow, they are essential for quantifying the strength of quadrupolar sources generated by unsteady flow in the wake, since the Lighthill tensor reduces to $T_{ij} \approx \rho u_i u_j$. The streamwise Reynolds stresses, referred to as τ_{uu}, are associated with flow recirculation and exhibit two different peak regions (Fig. 9a). The crosswise Reynolds stresses, referred to as τ_{vv}, are linked to the oscillatory motion of the flow and present a single peak region located where the large-scale vortices start to interact (Fig. 9b). Furthermore, the crosswise Reynolds stresses are larger than their streamwise counterparts by a factor of about 2. This result supports the hypothesis drawn in Section V.A concerning the dipolar pattern of wake sources. Indeed, the vortices undergo predominantly vertical acceleration, which coincides with the dipole's axis of maximum emission. Consequently, the TKE exhibits the same pattern as that observed for the crosswise Reynolds stresses, showing a single peak region where vortices start to interact (Fig. 9c) and where the origin of the volumetric sources is expected to be located [15].

To analyze the flow field within the porous medium, time-averaged streamwise velocity and TKE distributions are reported in Figs. 10a and 10b, respectively. The former clearly shows that a small wake region forms downstream of each small-scale cylinder, indicating that vortex shedding occurs as they interact with the free stream. Due to this phenomenon, the flow dissipates part of its kinetic energy as it penetrates the porous medium, which explains the low-energy region downstream of the surface shown in Fig. 8a. Furthermore, the wake generated by each small-scale cylinder in the windward region exhibits a significant level of TKE (Fig. 10b). This effect is most evident in the two outer layers, which are exposed to a velocity close to the free-stream value. In contrast, the inner layers may experience lower local velocities, resulting in a Reynolds number below the critical threshold for vortex shedding [13]. The data analysis reveals that the flow pattern downstream of each small-scale cylinder, particularly in the outer layers, resembles that of an isolated cylinder placed in the free stream. This observation supports the hypothesis presented in Section II.B regarding the high-frequency noise-generation mechanism, in which small-scale cylinders undergo vortex shedding, thereby generating tonal noise.

C. Coherence analysis

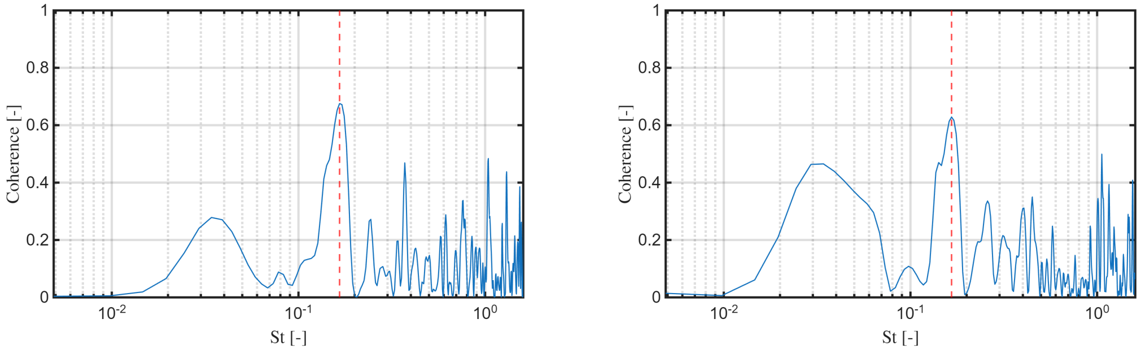

(a) **(b)**

Fig. 11 Coherence, computed using Eq. (12), between (a) crosswise and (b) streamwise velocity fluctuations at $(x, y, z) = (4.5D, 0.5D_{\mathbf{ext}}, 0)$ **and the far-field pressure at the microphone location** $(0, 1, 0)$, $[\mathrm{m}]$**, obtained using the FWH permeable formulation.**

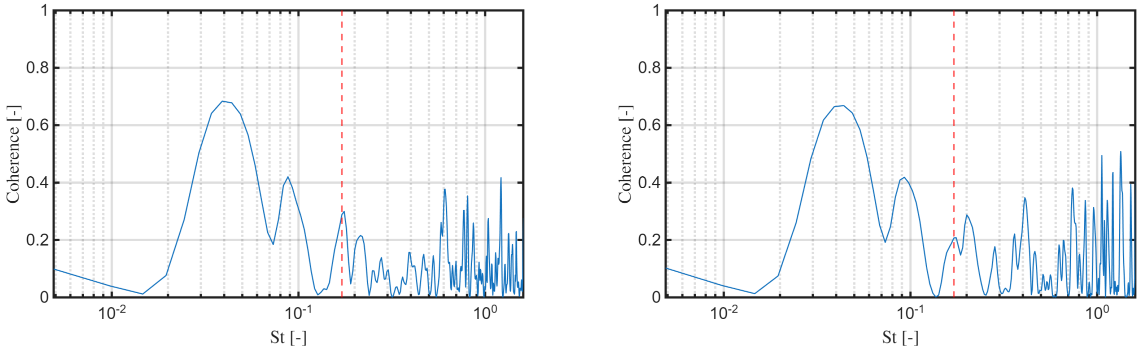

(a) **(b)**

Fig. 12 Coherence, computed using Eq. (12), between near-field pressure fluctuations at $\theta = 50^\circ$ **(a) and** $\theta = 90^\circ$ **(b), and the far-field pressure at the microphone position** $(0,\ 1,\ 0)$ $[\mathrm{m}]$**, based on the FWH permeable formulation (angles are defined such that** $\theta = 180^\circ$ **corresponds to the stagnation line).**

The relative contributions of volume and surface noise sources are assessed through the computation of the coherence between the far-field pressure, obtained from the FWH permeable formulation, and both components of the velocity fluctuations (denoted as $|\gamma|^2_{p,v}$ and $|\gamma|^2_{p,u}$ for the crosswise and streamwise components, respectively), and the near-field pressure (i.e., $|\gamma|^2_{p,p_s}$). This evaluation is carried out using Eq. (12), where a and b represent the time histories of the far-field pressure and the velocity fluctuations or the near-field pressure, respectively. The results are shown in Figs. 11

and 12. Because volume and surface noise sources contribute differently in the low-frequency range, as shown in Fig. 7a, only frequencies up to $St = 1$ are considered. Both $|\gamma|^2_{p,v}$ and $|\gamma|^2_{p,u}$ reach their peaks at the shedding frequency, highlighting their role in the direct propagation of acoustic waves associated with tonal noise generation. Additional peaks at different frequencies are attributed to spurious effects. At the shedding frequency, highlighted by the red dotted line, $|\gamma|^2_{p,v}$ (Fig. 11a) and $|\gamma|^2_{p,u}$ (Fig. 11b) are considerably higher than $|\gamma|^2_{p,p_s}$ for both locations considered on the cylinder surface (Figs. 12a and 12b). This result suggests that acoustic waves generated by volumetric wake sources exert a greater relative influence on the far field than those originating from the surface. This supports the scenario outlined in Section V.A concerning the role of volume sources in the noise radiated from a porous-coated cylinder. Moreover, it is observed that, at the shedding frequency, $|\gamma|^2_{p,u} < |\gamma|^2_{p,v}$, suggesting that crosswise velocity fluctuations play a more significant role in the tonal noise generation mechanism. This result, combined with the predominance of the crosswise Reynolds component analyzed in Section V.B, reinforces the theory presented in Section V.A concerning the dipolar nature of the wake sources. Similar trends are observed at different locations in the wake and on the surface, although they are not reported here for brevity.

VI. Conclusions

This paper elucidates the physical connection between near-wake developments and the noise mitigation performance of a structured porous-coated cylinder. To this end, a numerical dataset obtained from high-fidelity simulations based on the LBM method is used, considering the porous model SRS98 proposed by Wen et al. [17]. For the SPC configuration considered here, the acoustic field is dominated by a high-frequency peak associated with tonal noise generated by the small-scale cylinders of the porous medium.

Preliminary results suggest that, in the low-frequency range, the dominant noise originates from wake sources located at the onset of the vortex-shedding instability. This result is physically linked to the increase in the vortex-formation length, which, in equivalent terms, reduces the efficiency of scattering mechanisms at the cylinder surface and, consequently, the contribution of dipolar noise to the far field. The relevance of volumetric wake sources is further confirmed through an alternative approach based on coherence analysis.

These results indicate that, despite the low Mach number, wake sources must be taken into account for the accurate prediction of the noise radiated by a coated cylinder. This constitutes an initial validation of the theoretical considerations on flow-induced noise from porous-coated cylinders proposed by Zamponi et al. [15].

Future work will focus on a more comprehensive validation of the numerical setup, along with a rigorous theoretical formulation of the problem. In particular, the low-frequency noise generated by the porous cylinder will be analyzed within the framework of vortex sound theory, while the mechanisms underlying high-frequency noise generation will be systematically investigated.

References

[1] Strouhal, V., "Ueber eine besondere Art der Tonerregung," *Annalen der Physik und Chemie*, Vol. 241, No. 10, 1878, pp. 216–251. https://doi.org/10.1002/andp.18782411005.

[2] Sueki, T., Takaishi, T., Ikeda, M., and Arai, N., "Application of porous material to reduce aerodynamic sound from bluff bodies," *Fluid Dynamics Research*, Vol. 42, No. 1, 2010, p. 015004. https://doi.org/10.1088/0169-5983/42/1/015004.

[3] Liu, H., Wein, J., and Qu, Z., "Prediction of aerodynamic noise reduction by using open-cell metal foam," *Journal of Sound and Vibration*, Vol. 331, No. 7, 2012, pp. 1483–1497. https://doi.org/10.1016/j.jsv.2011.11.016.

[4] Geyer, T. F., and Sarradj, E., "Circular cylinders with soft porous cover for flow noise reduction," *Experiments in Fluids*, Vol. 57, No. 3, 2016, pp. 1–16. https://doi.org/10.1007/s00348-016-2119-7.

[5] Sadeghipour, S., Showkat Ali, S. A., Liu, X., Azarpeyvand, M., and Thorpe, G. R., "Control of flows around bluff bodies mediated by porous materials," *Experimental Thermal and Fluid Science*, Vol. 114, 2020, p. 110048. https://doi.org/10.1016/j.expthermflusci.2020.110048.

[6] Showkat Ali, S. A., Liu, X., and Azarpeyvand, M., "Bluff Body Flow and Noise Control Using Porous Media," *22nd AIAA/CEAS Aeroacoustics Conference*, Lyon, France, 2016, pp. 2016–2754. https://doi.org/10.2514/6.2016-2754.

[7] Xia, C., Wei, Z., Yuan, H., Li, Q., and Yang, Z., "POD analysis of the wake behind a circular cylinder coated with porous media," *Journal of Visualization*, Vol. 21, No. 4, 2018, pp. 965–985. https://doi.org/10.1007/s12650-018-0511-5.

[8] Naito, H., and Fukagata, K., “Numerical simulation of flow around a circular cylinder having porous surface,” *Physics of Fluids*, Vol. 24, No. 11, 2012, p. 117102. https://doi.org/10.1063/1.4767534.

[9] Sato, Y., and Hattori, Y., “Mechanism of reduction of aeroacoustic sound by porous material: comparative study of microscopic and macroscopic models,” *Journal of Fluid Mechanics*, Vol. 929, 2021, p. A34. https://doi.org/10.1017/jfm.2021.884.

[10] Arcondoulis, E. J. G., Liu, Y., Li, Z., Yang, Y., and Wang, Y., “Structured Porous Material Design for Passive Flow and Noise Control of Cylinders in Uniform Flow,” *Materials*, Vol. 12, No. 18, 2019, p. 2905. https://doi.org/10.3390/ma12182905.

[11] Arcondoulis, E. J. G., Liu, Y., Ragni, D., Avallone, F., Rubio-Carpio, A., Sedaghatizadeh, N., Yang, Y., and Li, Z., “Internal shear layer and vortex shedding development of a structured porous coated cylinder using tomographic particle image velocimetry,” *Journal of Fluid Mechanics*, Vol. 967, 2023, p. A17. https://doi.org/10.1017/jfm.2023.473.

[12] Liu, H., Wein, J., and Qu, Z., “Aerodynamic noise simulation of porous medium-coated cylinder: Broadband hump noise mechanism and effects of permeability and pores distribution on tonal noise,” *Journal of Sound and Vibration*, Vol. 607, 2025, p. 119046. https://doi.org/10.1016/j.jsv.2025.119046.

[13] Arcondoulis, E. J. G., Zamponi, R., Alagöz, I., Avallone, F., and Paruchuri, C., “High-Frequency Aeroacoustic Source Mechanisms of a Structured Porous Coated Cylinder,” *30th AIAA/CEAS Aeroacoustics Conference*, Rome, Italy, 2024, pp. 2024–3342. https://doi.org/10.2514/6.2024-3342.

[14] Zamponi, R., Moreau, S., and Schram, C., “Rapid distortion theory of turbulent flow around a porous cylinder,” *Journal of Fluid Mechanics*, Vol. 915, 2021, p. A27. https://doi.org/10.1017/jfm.2021.8.

[15] Zamponi, R., Avallone, F., Ragni, D., Schram, C., and van der Zwaag, S., “Relevance of quadrupolar sound diffraction on flow-induced noise from porous-coated cylinders,” *Journal of Sound and Vibration*, Vol. 583, 2024, p. 118430. https://doi.org/10.1016/j.jsv.2024.118430.

[16] Zamponi, R., Ragni, D., Van Der Zwaag, S., and Avallone, F., “Innovative coatings for reducing flow-induced cylinder noise by altering the sound diffraction,” *Phys. Fluids*, Vol. 35, No. 12, 2023, p. 127120. https://doi.org/10.1063/5.0177263.

[17] Wen, K., Arcondoulis, E. J. G., Li, Z., and Liu, Y., “Structure resolved simulations of flow around porous coated cylinders based on a simplified pore-scale model,” *Aerospace Science and Technology*, Vol. 119, 2021, p. 107181. https://doi.org/10.1016/j.ast.2021.107181.

[18] Crighton, D. G., and Leppington, F. G., “On the scattering of aerodynamic noise.” *Journal of Fluid Mechanics*, Vol. 46, No. 3, 1971, pp. 577–597. https://doi.org/10.1017/S0022112071000715.

[19] Gloerfelt, X., Pérot, F., Bailly, C., and Juvé, D., “Flow-induced cylinder noise formulated as a diffraction problem for low Mach numbers,” *Journal of Sound and Vibration*, Vol. 287, No. 1-2, 2005, pp. 129–151. https://doi.org/10.1016/j.jsv.2004.10.047.

[20] Lighthill, M. J., “On Sound Generated Aerodynamically. I. General Theory,” *Proceedings of the Royal Society of London. Series A. Mathematical and Physical Sciences*, Vol. 231, No. 1107, 1952, pp. 564–587. https://doi.org/10.1098/rspa.1952.0060.

[21] Curle, N., “The influence of solid boundaries upon aerodynamic sound,” *Proceedings of the Royal Society of London. Series A. Mathematical and Physical Sciences*, Vol. 231, No. 1187, 1955, pp. 501–514. https://doi.org/10.1098/rspa.1955.0191.

[22] Zamponi, R., Satcunanathan, S., Moreau, S., Meinke, M., Schröder, W., and Schram, C., “Effect of porosity on Curle’s dipolar sources on an aerofoil in turbulent flow,” *Journal of Sound and Vibration*, Vol. 542, 2023, p. 117353. https://doi.org/10.1016/j.jsv.2022.117353.

[23] Chen, H., Chen, S., and Matthaeus, W. H., “Recovery of the Navier-Stokes Equations Using a Lattice-Gas Boltzmann Method,” *Physical Review A*, Vol. 45, No. 8, 1992, pp. R5339–R5342. https://doi.org/10.1103/PhysRevA.45.R5339.

[24] Bhatnagar, P. L., Gross, E. P., and Krook, M., “A Model for Collision Processes in Gases. I. Small Amplitude Processes in Charged and Neutral One-Component Systems,” *Physical Review*, Vol. 94, No. 3, 1954, pp. 511–525. https://doi.org/10.1103/PhysRev.94.511.

[25] Lateb, M., Masson, C., Stathopoulos, T., and Bédard, C., “Comparison of various types of k–ε models for pollutant emissions around a two-building configuration,” *Journal of Wind Engineering and Industrial Aerodynamics*, Vol. 115, 2013, pp. 9–21. https://doi.org/10.1016/j.jweia.2013.01.001.

[26] Ffowcs Williams, J. E., and Hawkings, D. L., “Sound Generation by Turbulence and Surfaces in Arbitrary Motion,” *Philosophical Transactions of the Royal Society of London. Series A, Mathematical and Physical Sciences*, Vol. 264, No. 1151, 1969, pp. 321–342. https://doi.org/10.1098/rsta.1969.0031.

[27] Farassat, F., “Derivation of Formulations 1 and 1A of Farassat,” NASA Technical Memorandum NASA/TM-2007-214853, NASA, Washington, D.C., 2007. URL https://ntrs.nasa.gov/api/citations/20070010579/downloads/20070010579.pdf.

[28] Maryami, R., Arcondoulis, E. J. G., and Liu, Y., “Flow and aerodynamic noise control of a circular cylinder by local blowing,” *Philosophical Transactions of the Royal Society A*, Vol. 382, 2024, p. 20230356. https://doi.org/10.1017/jfm.2024.39.

[29] Zamponi, R., Avallone, F., Ragni, D., and van der Zwaag, S., “On the Aerodynamic-Noise Sources in a Circular Cylinder Coated with Porous Materials,” *28th AIAA/CEAS Aeroacoustics Conference*, Southampton, UK, 2022, pp. 2022–3042. https://doi.org/10.2514/6.2022-3042.